

Communication

# Nonstoichiometric Cu<sub>0.6</sub>Ni<sub>0.4</sub>Co<sub>2</sub>O<sub>4</sub> Nanowires as an Anode Material for High Performance Lithium Storage

Junhao Li <sup>1</sup>, Ningyi Jiang <sup>2,3,4</sup>, Jinyun Liao <sup>5</sup>, Yufa Feng <sup>5</sup>, Quanbing Liu <sup>1,\*</sup> and Hao Li <sup>5,\*</sup> 

<sup>1</sup> School of Chemical Engineering and Light Industry, Guangdong University of Technology, Guangzhou 510006, China; ljh15626204622@163.com

<sup>2</sup> School of Chemical Engineering and Technology, Tianjin University, Tianjin 300072, China; nyjiang18@163.com

<sup>3</sup> Tianjin Institute of Power Sources, Tianjin 30084, China

<sup>4</sup> Tianjin Space Power Technology Co., Ltd., Tianjin 30084, China

<sup>5</sup> School of chemistry and Materials Engineering, Huizhou University, Huizhou 516007, China; jyliao@126.com (J.L.); yufafeng@126.com (Y.F.)

\* Correspondence: liuqb@gdut.edu.cn (Q.L.); lihao180@126.com (H.L.);  
Tel.: +86-020-39322231 (Q.L.); +86-752-2527229 (H.L.)

Received: 27 November 2019; Accepted: 17 January 2020; Published: 22 January 2020



**Abstract:** Transition metal oxide is one of the most promising anode materials for lithium-ion batteries. Generally, the electrochemical property of transition metal oxides can be improved by optimizing their element components and controlling their nano-architecture. Herein, we designed nonstoichiometric Cu<sub>0.6</sub>Ni<sub>0.4</sub>Co<sub>2</sub>O<sub>4</sub> nanowires for high performance lithium-ion storage. It is found that the specific capacity of Cu<sub>0.6</sub>Ni<sub>0.4</sub>Co<sub>2</sub>O<sub>4</sub> nanowires remain 880 mAh g<sup>-1</sup> after 50 cycles, exhibiting much better electrochemical performance than CuCo<sub>2</sub>O<sub>4</sub> and NiCo<sub>2</sub>O<sub>4</sub>. After experiencing a large current charge and discharge state, the discharge capacity of Cu<sub>0.6</sub>Ni<sub>0.4</sub>Co<sub>2</sub>O<sub>4</sub> nanowires recovers to 780 mAh g<sup>-1</sup> at 50 mA g<sup>-1</sup>, which is ca. 88% of the initial capacity. The high electrochemical performance of Cu<sub>0.6</sub>Ni<sub>0.4</sub>Co<sub>2</sub>O<sub>4</sub> nanowires is related to their better electronic conductivity and synergistic effect of metals. This work may provide a new strategy for the design of multicomponent transition metal oxides as anode materials for lithium-ion batteries.

**Keywords:** lithium-ion battery; anode material; nonstoichiometric; doping; Cu<sub>0.6</sub>Ni<sub>0.4</sub>Co<sub>2</sub>O<sub>4</sub> nanowires

## 1. Introduction

Lithium-ion batteries (LIB) have many advantages, such as high energy density, excellent cycle stability, no memory effect, and so on [1]. They are widely used in many fields, such as electronic products, electric vehicles, and energy storage system, which have greatly improved modern humans' lives [2]. The energy density of LIB is closely related to the lithium storage performance and voltage of the anode materials. The transition metal oxide Co<sub>3</sub>O<sub>4</sub> used as a promising anode material for lithium-ion batteries, first reported by Poizot [3] in 2000, has attracted extensive interest of researchers with 890 mAh g<sup>-1</sup> theoretical capacity, which is much higher than commercial graphite (372 mAh g<sup>-1</sup>). Different from lithium intercalation mechanism of graphite, Co<sub>3</sub>O<sub>4</sub> is based on a conversion reaction as anode materials transforms into metallic cobalt, with great volume expansion and metal reunion during lithiation/deithiation [4].

Due to the inherent defects of the material, many researchers attempt to enhance the electrochemical performance of Co<sub>3</sub>O<sub>4</sub> by controlling their microstructures and optimizing their components [5]. On the one hand, great efforts have been devoted to the morphological control of Co<sub>3</sub>O<sub>4</sub>, and therefore, many of

the different shaped  $\text{Co}_3\text{O}_4$  nanostructures, such as peapod-like [6], yolk-shell [7], hollow nanofibers [8], nanowires [9,10], other complex structures [11–18] have been developed and applied as anode materials in lithium-ion batteries. Compared with other nanostructures, nanowires have large open space, which allows electrolytes to diffuse into the electrode inner region and shorten the solid-phase diffusion path of lithium ions. Moreover, the mechanical flexibility and Young's modulus of nanowires are significant for micro-flexible electronic components [19]. For example, Guan [9] synthesized 1D  $\text{Co}_3\text{O}_4$  mesoporous nanowires, grown on Ni foam, whose specific capacity was approximately  $1600 \text{ mAh g}^{-1}$  at current density of  $0.5 \text{ A g}^{-1}$ . Zeng [20] designed quasi-single-crystalline mesoporous  $\text{Co}_3\text{O}_4$  and  $\text{CoO}$  nanowires from precursor  $\text{Co}(\text{Co}_3)_{0.5}(\text{OH})$  and the  $\text{CoO}$  nanowires remain nearly 100% capacity retention after 70 cycles.

On the other hand, it is a viable strategy to design transition-metal oxide composites for enhancing lithium storage performance [21]. It has been reported that the composites of bimetal oxide showed much higher electrochemical performance than the single ones due to low activation energy for electron transfer between cations [10,22,23].  $\text{MCu}_2\text{O}_4$  ( $\text{M} = \text{Ni}$  [24–27],  $\text{Cu}$  [28],  $\text{Fe}$  [29],  $\text{Zn}$  [30],  $\text{Mn}$  [31]) have been widely used as anode materials over the last few years. Lou [26] synthesized  $\text{NiCo}_2\text{O}_4$  complex hollow spheres as anode material in lithium-ion battery and its specific capacity was  $1400 \text{ mAh g}^{-1}$  at  $150 \text{ mA g}^{-1}$  with great cycling stability. Jiang [32] reported  $\text{CuCo}_2\text{O}_4$  nanoparticle showed high reversible capacity of  $1040 \text{ mAh g}^{-1}$  at  $0.1 \text{ C}$ . Cao [33] designed ultrathin  $\text{ZnCo}_2\text{O}_4$  nanosheets for lithium anode with excellent long life (about  $900 \text{ mAh g}^{-1}$  after 200 cycles at  $200 \text{ mA g}^{-1}$  current density).

Herein, we report nonstoichiometric  $\text{Cu}_{0.6}\text{Ni}_{0.4}\text{Co}_2\text{O}_4$  nanowires, which can be regarded as a composite of  $\text{CuCo}_2\text{O}_4$  and  $\text{NiCo}_2\text{O}_4$ , as an anode material in lithium-ion battery. As we know, such composites, as an anode material in lithium-ion area has not been reported yet. Owing to the relatively low activation energy for electron transfer between  $\text{Cu}^{2+}/\text{Cu}$ ,  $\text{Ni}^{2+}/\text{Ni}^{3+}$  and  $\text{Co}^{2+}/\text{Co}^{3+}$ , the electronic conductivity and cycling stability for  $\text{Cu}_{0.6}\text{Ni}_{0.4}\text{Co}_2\text{O}_4$  nanowires are significantly improved. In the first cycle, discharge and charge capacities are  $1120 \text{ mAh g}^{-1}$  and  $972 \text{ mAh g}^{-1}$  at  $50 \text{ mA g}^{-1}$ , respectively. After 50 cycles, the specific capacity of  $\text{Cu}_{0.6}\text{Ni}_{0.4}\text{Co}_2\text{O}_4$  nanowires remain  $880 \text{ mAh g}^{-1}$  and the coulombic efficiency is approximately 100%.

## 2. Experimental

### 2.1. Synthesis of Anode Materials

All the reagents (Tianjin Damo Chemical Reagent Factory, Tianjin, China) were analytically pure without further treatment. Similar preparation methods could be referred to our previous work [34]. To prepare the  $\text{Cu}_{0.6}\text{Ni}_{0.4}\text{Co}_2\text{O}_4$  nanowires, 4 mmol cobalt acetate was dissolved in 30 mL ultrapure water. Subsequently, 4 mmol lauryl sodium sulfate, 1.2 mmol copper chloride, and the 0.8 mmol nickel chloride were added to the above cobalt acetate solution in sequence. Then, 48 mmol hexamethylenetetramine was dissolved in 30 mL ultrapure water to form a transparent solution which was dropped into the above mixed solution slowly. After stirring for 1 h, the resultant solution was poured into a 100 mL Teflon-lined stainless autoclave. Then the autoclave was heated at  $120^\circ\text{C}$  for 12 h in oven. The obtained sediment was filtered, rinsed and dried. Finally, after calcination of the powder at  $600^\circ\text{C}$  for 2 h in muffle,  $\text{Cu}_{0.6}\text{Ni}_{0.4}\text{Co}_2\text{O}_4$  was obtained. Similarly,  $\text{NiCo}_2\text{O}_4$  and  $\text{CuCo}_2\text{O}_4$  were obtained by adjusting the addition amount of copper chloride and nickel chloride.

### 2.2. Characterizations

Crystal information of the samples was acquired by Bruker D8 Discover X-ray diffractometer (XRD, Tokyo, Japan) with  $\text{Cu K}\alpha$  radiation ( $\lambda = 1.5406\text{\AA}$ ). Microstructures, particle sizes and element mapping were analyzed by using a JEOL-7100F field-emission scanning electron microscope (FESEM, Hitachi, Japan). Interior structure was observed by a JEOL JEM-2100F transmission electron microscope (TEM, FEI, Hillsboro, OR, USA). The elements and chemical states of the sample were analyzed by a Kratos Axis Ultra DLD X-ray photoelectron spectrometer (XPS, VG, Manchester, UK). The molar ratios

were determined with an Agilent 7800 Inductively Coupled Plasma (ICP) Mass Spectrometry (Thermo Fisher, Waltham, MA, USA).

### 2.3. Electrochemical Performance Test

The 2032-coin battery is assembled in a glove box filled with inert atmosphere for electrochemical performance test. The fabricated electrode consisted of active materials, acetylene black, polyvinylidene fluoride (PVDF) with a mass ratio of 7:2:1. Each component was well mixed to form a paste, which was coated on copper foil current collector. The loading on the electrode is approximately  $1 \text{ mg cm}^{-2}$ . The electrolyte used was 1.0 M LiPF<sub>6</sub> in a 50:50 (w/w) mixture of ethylene carbonate (EC) and diethyl carbonate (DEC). The specific capacity of the battery was tested by cyclic charge and discharge between 0–3 V (Land CT2001A, Hubei, China). The cyclic voltammetry and electrochemical impedance test were obtained by using an electrochemical workstation (CHI 760E, CH Instrument Ins., Shanghai, China).

## 3. Results and Discussion

The X-ray diffraction (XRD) patterns of the NiCo<sub>2</sub>O<sub>4</sub>, CuCo<sub>2</sub>O<sub>4</sub>, and Cu<sub>0.6</sub>Ni<sub>0.4</sub>Co<sub>2</sub>O<sub>4</sub> powders are shown in Figure 1. It is discovered that the characteristic peaks of the NiCo<sub>2</sub>O<sub>4</sub> and CuCo<sub>2</sub>O<sub>4</sub> are very similar. All the diffraction peaks of the NiCo<sub>2</sub>O<sub>4</sub>, CuCo<sub>2</sub>O<sub>4</sub> powders correspond to the (220), (311), (222), (400), (422), (511), and (440) plane reflections of cubic spinel NiCo<sub>2</sub>O<sub>4</sub> or CuCo<sub>2</sub>O<sub>4</sub>. Cu<sub>0.6</sub>Ni<sub>0.4</sub>Co<sub>2</sub>O<sub>4</sub> has similar characteristic peaks as NiCo<sub>2</sub>O<sub>4</sub> [35] and CuCo<sub>2</sub>O<sub>4</sub>. We can regard Cu<sub>0.6</sub>Ni<sub>0.4</sub>Co<sub>2</sub>O<sub>4</sub> as a composite of NiCo<sub>2</sub>O<sub>4</sub> and CuCo<sub>2</sub>O<sub>4</sub> [36]. The peak at 25° for anode materials is attributed to the disorderedly stacked carbon, derived from incomplete decomposition of organic ingredients [37]. There is a small peak in NiCo<sub>2</sub>O<sub>4</sub> at 44° indexing as NiO (JCPDS NO. 65-2901), which is also found in previous literature [38]. The peak at 33° for CuCo<sub>2</sub>O<sub>4</sub> may be indexed as CuO (JCPDS NO. 44-0706). According to the Scherer's formula, the average crystal size of a material can be calculated [39,40],

$$D = 0.89\lambda / (\beta \cos \theta) \quad (1)$$

where  $D$  is the average grain size,  $\lambda$  is X-ray wavelength and constant of 0.154 nm,  $\beta$  is half-height width of diffraction peak, and  $\theta$  is Bragg diffraction angle. The average crystalline sizes of NiCo<sub>2</sub>O<sub>4</sub> and CuCo<sub>2</sub>O<sub>4</sub> are 16.5, and 24.9 nm, respectively. Meanwhile, that of Cu<sub>0.6</sub>Ni<sub>0.4</sub>Co<sub>2</sub>O<sub>4</sub> is 18.0 nm, which is between 16.5 nm and 24.9 nm, indicating that the formation of composite of NiCo<sub>2</sub>O<sub>4</sub> and CuCo<sub>2</sub>O<sub>4</sub> will not result in a pronounced change in crystalline size.

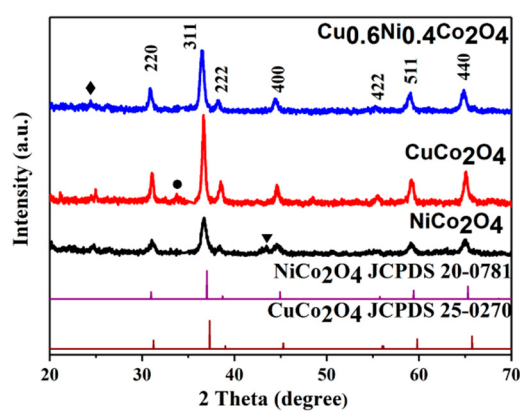


**Figure 1.** X-ray diffraction (XRD) pattern of the NiCo<sub>2</sub>O<sub>4</sub>, CuCo<sub>2</sub>O<sub>4</sub>, and Cu<sub>0.6</sub>Ni<sub>0.4</sub>Co<sub>2</sub>O<sub>4</sub> powders.

Scanning electron microscopy (SEM) images are used to observe the morphology and structures of materials, as shown in Figure 2. Apparently, the samples of the NiCo<sub>2</sub>O<sub>4</sub> and Cu<sub>0.6</sub>Ni<sub>0.4</sub>Co<sub>2</sub>O<sub>4</sub> consist of nanowires with an average diameter of ca. 50 nm. Interestingly, all these nanowires are assembled

by small nanoparticles. The structure of  $\text{CuCo}_2\text{O}_4$  is nanoparticles with an average diameter of ca. 30 nm. The TEM images of three anode materials in Figure 3, present the inner structures for  $\text{NiCo}_2\text{O}_4$ ,  $\text{Cu}_{0.6}\text{Ni}_{0.4}\text{Co}_2\text{O}_4$ , and  $\text{CuCo}_2\text{O}_4$ . The anode materials are solid instead of hollow. Besides, inner structure of  $\text{Cu}_{0.6}\text{Ni}_{0.4}\text{Co}_2\text{O}_4$  is similar with  $\text{NiCo}_2\text{O}_4$  rather than  $\text{CuCo}_2\text{O}_4$ . Figure 3g is high resolution transmission electron microscope (HRTEM) images of the  $\text{Cu}_{0.6}\text{Ni}_{0.4}\text{Co}_2\text{O}_4$ . The lattice spacing of ca. 0.23 nm, 0.2 nm, 0.28 nm, and 0.24 nm can be seen, corresponding to the crystal surfaces (222), (400), (220), and (311) planes of cubic spinel  $\text{Cu}_{0.6}\text{Ni}_{0.4}\text{Co}_2\text{O}_4$ . Element mapping of  $\text{Cu}_{0.6}\text{Ni}_{0.4}\text{Co}_2\text{O}_4$  is measured in Figure 4. The elements of Co, Ni, Cu, and O can be found in the mapping picture, indicating that these elements are uniformly distributed. The result of ICP measure shows the ratio of Cu, Ni, and Co is 0.61:0.41:1.99, which are well match with the designed values.

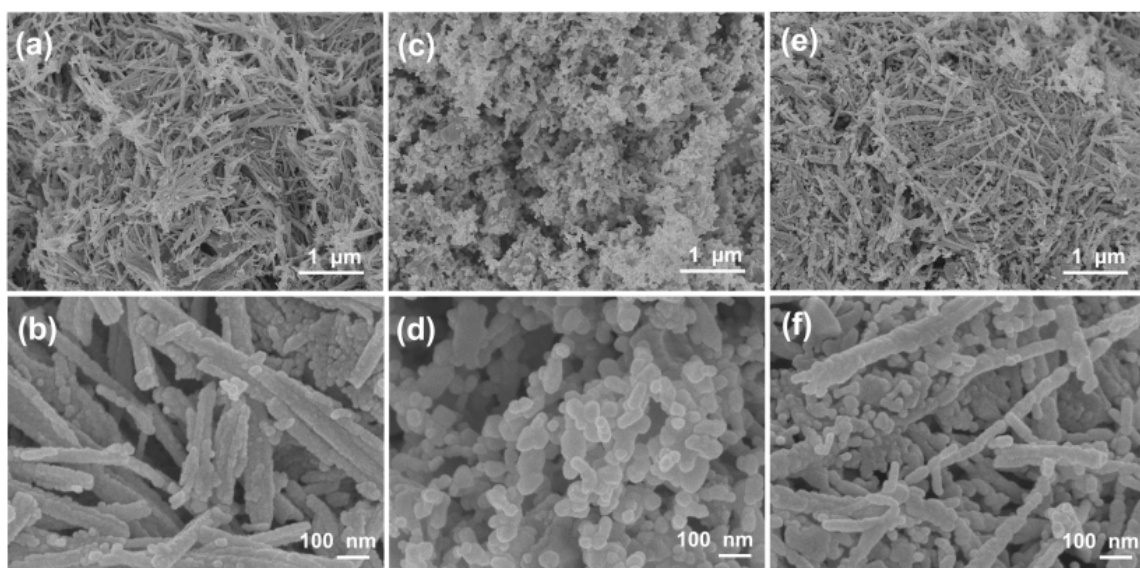


**Figure 2.** Scanning electron microscopy (SEM) images of (a,b)  $\text{NiCo}_2\text{O}_4$ , (c,d)  $\text{CuCo}_2\text{O}_4$  and (e,f)  $\text{Cu}_{0.6}\text{Ni}_{0.4}\text{Co}_2\text{O}_4$ .

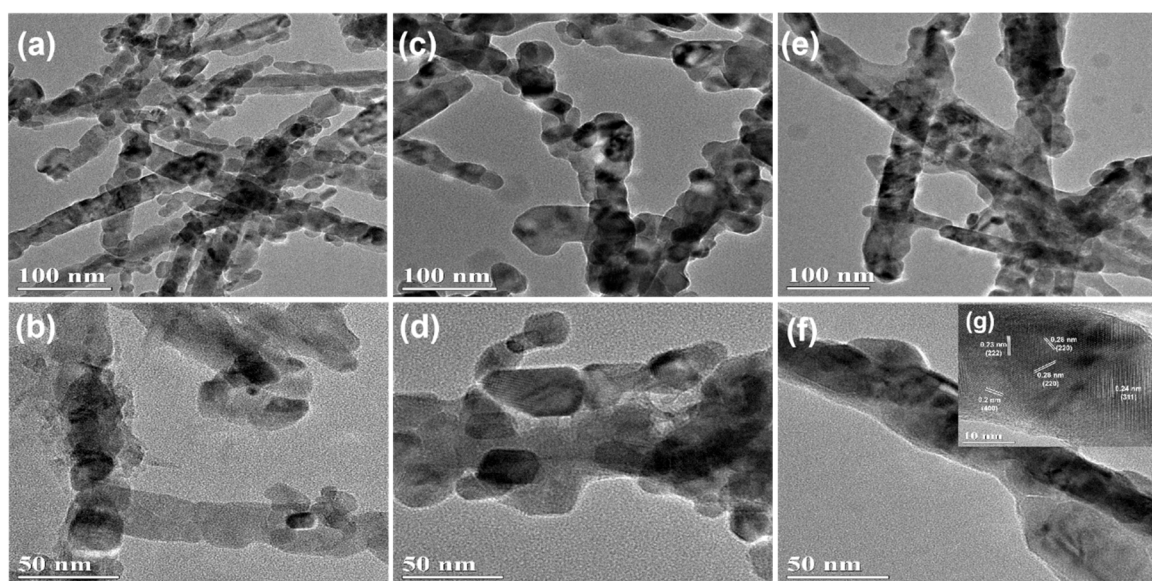


**Figure 3.** Transmission electron microscopy (TEM) image of (a,b)  $\text{NiCo}_2\text{O}_4$ , (c,d)  $\text{CuCo}_2\text{O}_4$  and (e,f)  $\text{Cu}_{0.6}\text{Ni}_{0.4}\text{Co}_2\text{O}_4$ ; (g) the inset showing the HRTEM image of  $\text{Cu}_{0.6}\text{Ni}_{0.4}\text{Co}_2\text{O}_4$ .

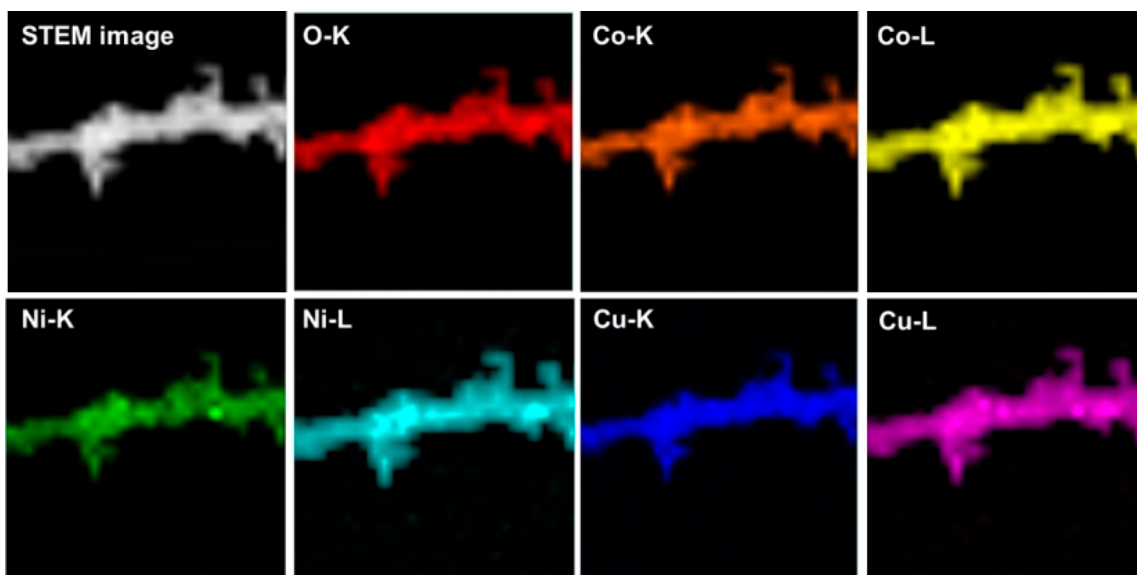


**Figure 4.** Elementary mapping of  $\text{Cu}_{0.6}\text{Ni}_{0.4}\text{Co}_2\text{O}_4$ .

In order to investigate the elements and chemical states on the surface of the anode materials, XPS analysis is carried out and the results are shown in Figure 5. In the XPS survey spectrum of  $\text{Cu}_{0.6}\text{Ni}_{0.4}\text{Co}_2\text{O}_4$  (Figure 5c), the signals of elements of Co, Ni, and Cu can be observed, which was different from those of  $\text{NiCo}_2\text{O}_4$  and  $\text{CuCo}_2\text{O}_4$  (Figure 5a,b), as the former has both Cu and Ni elements, and the three transition elements Cu, Ni, and Co will affect the outer electronic structure of each other. As shown in Figure 5a,b, no signal of Ni is found in  $\text{CuCo}_2\text{O}_4$ , while the Cu signal was absent in  $\text{NiCo}_2\text{O}_4$ , which are as expected. Figure 5d–f is the Ni 2p, Cu 2p, and Co 2p spectrum of the anode materials, respectively. There are six peaks in Ni 2p spectrum for  $\text{NiCo}_2\text{O}_4$  and  $\text{Cu}_{0.6}\text{Ni}_{0.4}\text{Co}_2\text{O}_4$ . The peaks are at 854.2 eV and 871.5 eV of  $\text{Ni}^{2+}$ , and 855.8 eV and 872.8 eV of  $\text{Ni}^{3+}$  for  $\text{Cu}_{0.6}\text{Ni}_{0.4}\text{Co}_2\text{O}_4$ . Comparing to the peaks for  $\text{NiCo}_2\text{O}_4$ , binding energy of Ni 2p for  $\text{Cu}_{0.6}\text{Ni}_{0.4}\text{Co}_2\text{O}_4$  are stronger. The peak areas mean the relative content of element valence. It's noted that the peak area of them is various, which shows the relative content of  $\text{Ni}^{2+}$  is lower in  $\text{Cu}_{0.6}\text{Ni}_{0.4}\text{Co}_2\text{O}_4$ . It indicates the amount of  $\text{Ni}^{2+}$  decreases in the presence of  $\text{Cu}^{2+}$ . There are four peaks in Cu 2p spectrum for  $\text{CuCo}_2\text{O}_4$  and  $\text{Cu}_{0.6}\text{Ni}_{0.4}\text{Co}_2\text{O}_4$ , indicating copper is divalent. Six peaks of Co 2p for the three materials can be found, manifesting the cobalt is trivalent and divalent. Similar, binding energy of Cu 2p, Co 2p for  $\text{Cu}_{0.6}\text{Ni}_{0.4}\text{Co}_2\text{O}_4$  are stronger than  $\text{CuCo}_2\text{O}_4$ , and  $\text{NiCo}_2\text{O}_4$ , respectively. The peak positions are corresponding to previous reports [32,39,41], indicating that  $\text{Cu}_{0.6}\text{Ni}_{0.4}\text{Co}_2\text{O}_4$  is prepared successfully and  $\text{Cu}^{2+}$  reduces the content of  $\text{Ni}^{2+}$ . The electron density of  $\text{Cu}_{0.6}\text{Ni}_{0.4}\text{Co}_2\text{O}_4$  in the outermost shell is affected by doping elements.

Transition metal oxides undergo a conversion reaction in the lithiation, with the change in metal valence and the formation of solid electrolyte interface (SEI) layer and  $\text{Li}_2\text{O}$  [3]. Figure 6 shows the CV test of  $\text{NiCo}_2\text{O}_4$ ,  $\text{CuCo}_2\text{O}_4$ , and  $\text{Cu}_{0.6}\text{Ni}_{0.4}\text{Co}_2\text{O}_4$  anode electrodes for the first three curves at a scan of  $0.2 \text{ mV s}^{-1}$  between 0.01 and 3 V. For the  $\text{NiCo}_2\text{O}_4$  anode material, during the first scan, the main cathodic peaks locate in 0.7 V corresponding to the reduction of  $\text{NiCo}_2\text{O}_4$  to metallic Ni and Co (Equation (2)), and the broad peaks at ca. 0.37 V corresponds to SEI layer [42]. The anode peaks are at the 1.63 V and 2.3 V, corresponding to oxidation of metallic  $\text{Ni}^0$  to  $\text{Ni}^{2+}$  and Co to  $\text{Co}^{3+}$ , respectively. (Equations (5), (7) and (8)). For the  $\text{CuCo}_2\text{O}_4$ , during the initial scan, the main cathodic peaks locate in 0.75 V, corresponding to the reduction of  $\text{CuCo}_2\text{O}_4$  to metallic Cu and Co (Equation (3)). It is mentioned that there are two peaks at ~0.5 V and ~0.6 V, revealing formation of SEI layer. The anode peaks were at the 1.1 V, 1.5 V and 2.2 V, corresponding to oxidation of metallic Cu and Co to  $\text{CuCo}_2\text{O}_4$  (Equations (6), (7) and (8), respectively). For  $\text{Cu}_{0.6}\text{Ni}_{0.4}\text{Co}_2\text{O}_4$ , during the first scan, the main cathodic peaks locate in 1.2 V and 0.8 V, assigning to reduction of metal oxide and formation of SEI film (Equation (4)).

The anode peaks are at the 1.63 V and 2.3 V, corresponding to oxidation of metallic Ni, Cu and Co to  $\text{Cu}_{0.6}\text{Ni}_{0.4}\text{Co}_2\text{O}_4$  (Equations (5)–(8)). At the same time, the peaks of  $\text{Cu}_{0.6}\text{Ni}_{0.4}\text{Co}_2\text{O}_4$  are narrower and stronger than those of  $\text{NiCo}_2\text{O}_4$  and  $\text{CuCo}_2\text{O}_4$ . This can be due to co-work of Co, Cu, and Ni, which stabilizes the structure and enhance the electronic conductivity in the process of electrochemical reaction, resulting in a longer cycle life and a lower potential polarization. The different positions of the peaks reveal that the REDOX potential can be changed slightly by composition and content of metal oxide in the chemical reaction. The first cathodic scan of the three anode materials, in addition to the reduction of metals, the formation of SEI film and  $\text{Li}_2\text{O}$  were occurred, so the second anode scan is quite different from the first one [43,44]. While, the second cycle anode scan of the three materials is roughly the same as the first cycle, demonstrating good cycle performance. The total reaction equations during charging and discharging are described as following:

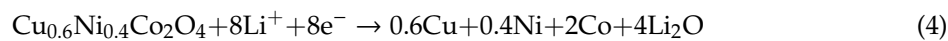
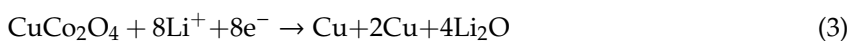
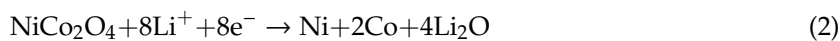
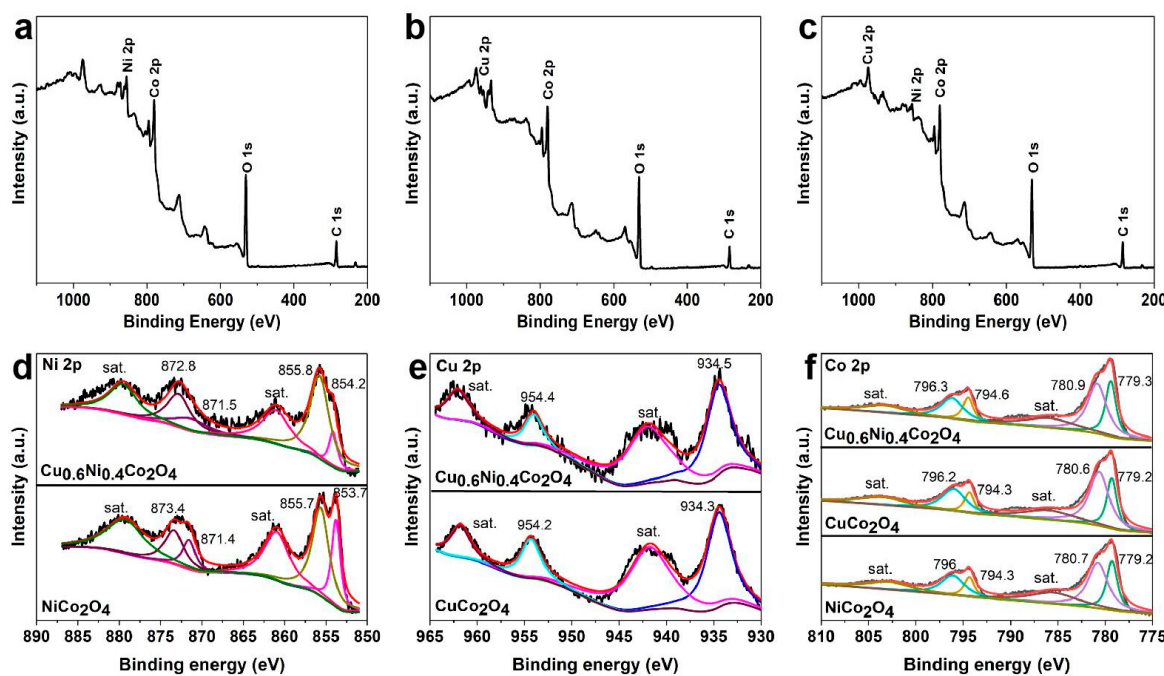
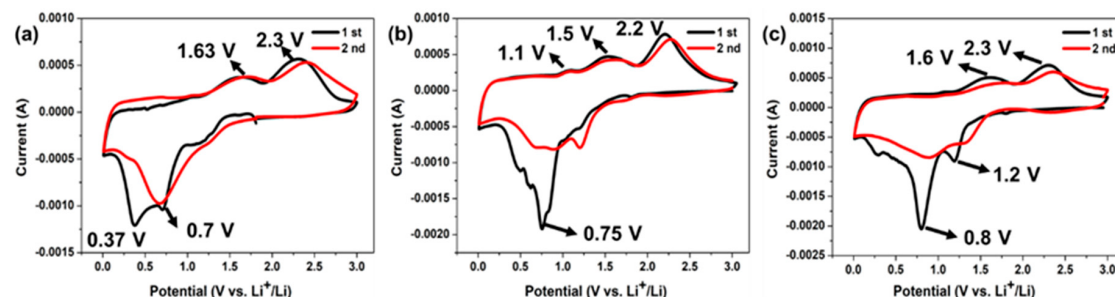


Figure 7 shows specific capacities of the  $\text{NiCo}_2\text{O}_4$ ,  $\text{CuCo}_2\text{O}_4$ ,  $\text{Cu}_{0.6}\text{Ni}_{0.4}\text{Co}_2\text{O}_4$  at the current density of 50 mA g<sup>-1</sup> between 0.01 and 3 V (vs.  $\text{Li}^+/\text{Li}$ ). The first discharge specific capacities of  $\text{NiCo}_2\text{O}_4$ ,  $\text{CuCo}_2\text{O}_4$ , and  $\text{Cu}_{0.6}\text{Ni}_{0.4}\text{Co}_2\text{O}_4$  are 950, 901, and 1120 mAh g<sup>-1</sup>, respectively (Figure 7a). The first charge specific capacities of  $\text{NiCo}_2\text{O}_4$ ,  $\text{CuCo}_2\text{O}_4$ , and  $\text{Cu}_{0.6}\text{Ni}_{0.4}\text{Co}_2\text{O}_4$  are 785, 633, and 972 mAh g<sup>-1</sup>, there are large specific capacity losses in the first charge/discharge cycle. We attribute them to some irreversible electrochemical reactions, including the SEI film formation, electrolyte decomposition, and so on. This phenomenon can be observed for most anode materials, which leads to the low coulombic efficiency in the first cycle and explains a large difference in the peak position of the reduction peak between the first and the second cycles in the CV test. The  $\text{NiCo}_2\text{O}_4$  electrode shows a specific discharge capacity of 743 mAh g<sup>-1</sup> in second cycle, and the specific capacity declines to 245 mAh g<sup>-1</sup> after 50 cycles. The  $\text{CuCo}_2\text{O}_4$  electrode shows a specific discharge capacity of 690 mAh g<sup>-1</sup> at the second cycle, while the specific capacity is attenuated to 375 mAh g<sup>-1</sup> after 50 cycles. The  $\text{Cu}_{0.6}\text{Ni}_{0.4}\text{Co}_2\text{O}_4$ , which can be regarded as a compound of  $\text{CuCo}_2\text{O}_4$  and  $\text{NiCo}_2\text{O}_4$ , exhibits the excellent electrochemical performance. The specific discharge capacity of  $\text{Cu}_{0.6}\text{Ni}_{0.4}\text{Co}_2\text{O}_4$  is maintained 880 mAh g<sup>-1</sup> from the second to the fiftieth cycle, and the coulombic efficiency close to 100%. As shown in Figure 7b, the change of the specific capacity of the three samples with the number of cycles is clearly visible. The capacities of  $\text{NiCo}_2\text{O}_4$  and  $\text{CuCo}_2\text{O}_4$  material go through a huge decay after 20 cycles, which is due to material pulverization. Meanwhile,  $\text{Cu}_{0.6}\text{Ni}_{0.4}\text{Co}_2\text{O}_4$ 's capacity has been well-maintained. The electrochemical stability is significantly improved because of better electronic conductivity of  $\text{Cu}_{0.6}\text{Ni}_{0.4}\text{Co}_2\text{O}_4$  and the synergistic effect of the elements. Due to the various insertion voltages for the metal oxides, the other inactive metal oxides can be “volume-buffering reservoir” to release volume stress when the active metal oxide is in a lithiation/delithiation process at a certain voltage [45]. The capacity rate performance of  $\text{Cu}_{0.6}\text{Ni}_{0.4}\text{Co}_2\text{O}_4$  was also studied and the results are showed in Figure 7c. The charge/discharge current density gradually increases to 2000 mA g<sup>-1</sup> and then returns to 50 mA g<sup>-1</sup>. The charge-discharge voltage platform was found to be almost kept same. The stable reversible discharge capacities decrease from 830 to 150 mAh g<sup>-1</sup> as the current density increases from 200 mA g<sup>-1</sup> to 2000 mA g<sup>-1</sup>. Furthermore, when the current density is restored to 50 mA g<sup>-1</sup>, the discharge capacity is 780 mAh g<sup>-1</sup>, which is ca. 88% of the initial

discharge capacity. These results demonstrate that the  $\text{Cu}_{0.6}\text{Ni}_{0.4}\text{Co}_2\text{O}_4$  has a better rate performance and a higher cycling stability.



**Figure 5.** XPS spectra of (a)  $\text{NiCo}_2\text{O}_4$ , (b)  $\text{CuCo}_2\text{O}_4$ , (c)  $\text{Cu}_{0.6}\text{Ni}_{0.4}\text{Co}_2\text{O}_4$  and (d) Ni 2p of  $\text{NiCo}_2\text{O}_4$  and  $\text{Cu}_{0.6}\text{Ni}_{0.4}\text{Co}_2\text{O}_4$ , (e) Cu 2p of  $\text{CuCo}_2\text{O}_4$  and  $\text{Cu}_{0.6}\text{Ni}_{0.4}\text{Co}_2\text{O}_4$ , (f) Co 2p of the three materials.



**Figure 6.** Cyclic voltammetry measure of (a)  $\text{NiCo}_2\text{O}_4$ , (b)  $\text{CuCo}_2\text{O}_4$ , and (c)  $\text{Cu}_{0.6}\text{Ni}_{0.4}\text{Co}_2\text{O}_4$ .

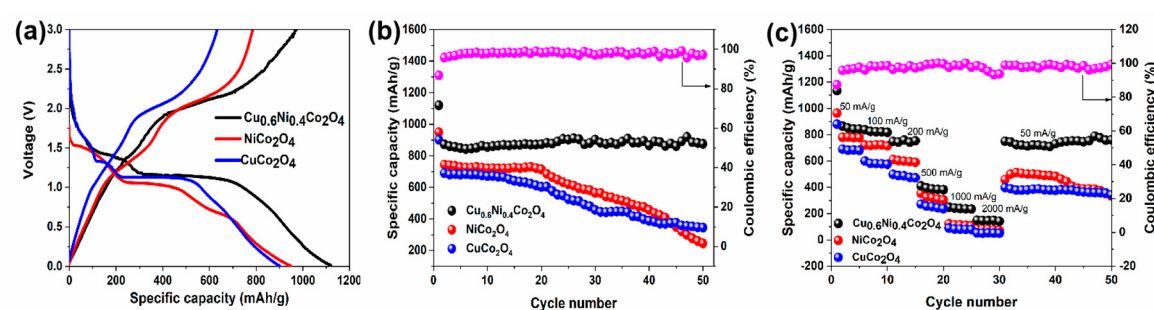


**Figure 7.** Electrochemical tests of the three samples: (a) Initial charge and discharge curves profiles for  $\text{NiCo}_2\text{O}_4$ ,  $\text{CuCo}_2\text{O}_4$ ,  $\text{Cu}_{0.6}\text{Ni}_{0.4}\text{Co}_2\text{O}_4$  at the current of  $50 \text{ mA g}^{-1}$  between 0.01 and 3 V (vs.  $\text{Li}^+/\text{Li}$ ). (b) Cycling performance of the three powders at a current of  $50 \text{ mA g}^{-1}$ . (c) Capacity rate performance of the anode materials.

To further compare the properties of the materials and the modification effects. The charge transfer behaviors of  $\text{NiCo}_2\text{O}_4$ ,  $\text{CuCo}_2\text{O}_4$ , and  $\text{Cu}_{0.6}\text{Ni}_{0.4}\text{Co}_2\text{O}_4$  are measured according to electrochemical

impedance spectroscopies (EIS). The Nyquist plots of the electrodes, with frequency range between 0.01 Hz to 100 kHz are shown in Figure 8. All plots make up a semicircle and a sloped line, the fitting circuit is shown insert. In the high intermediate frequency region, the diameter of the semicircle indicates charge transfer resistance ( $R_{ct}$ ) in the interface between the electrolyte and grains of active material [46]. It is easy to see that the diameter of the semicircle of  $\text{Cu}_{0.6}\text{Ni}_{0.4}\text{Co}_2\text{O}_4$  is much smaller than the diameter of  $\text{NiCo}_2\text{O}_4$  and  $\text{CuCo}_2\text{O}_4$ . The electron transfer resistance of  $\text{Cu}_{0.6}\text{Ni}_{0.4}\text{Co}_2\text{O}_4$  (120  $\Omega$ ) is less than of  $\text{NiCo}_2\text{O}_4$  (300  $\Omega$ ) and  $\text{CuCo}_2\text{O}_4$  (380  $\Omega$ ), which shows  $\text{Cu}_{0.6}\text{Ni}_{0.4}\text{Co}_2\text{O}_4$  sample has the lowest charge-transfer resistance. The low-frequency line stands for the Warburg resistance ( $W$ ) related to the lithium ions diffusion in electrode materials. The line slope of  $\text{Cu}_{0.6}\text{Ni}_{0.4}\text{Co}_2\text{O}_4$  is larger than of  $\text{NiCo}_2\text{O}_4$  and  $\text{CuCo}_2\text{O}_4$ , indicating faster solid-state diffusion of lithium ion is in the  $\text{Cu}_{0.6}\text{Ni}_{0.4}\text{Co}_2\text{O}_4$ . This evidence further proves that  $\text{Cu}_{0.6}\text{Ni}_{0.4}\text{Co}_2\text{O}_4$  has better electrochemical performance and lower charge transfer resistance due to co-work of  $\text{Cu}^{2+}$ ,  $\text{Ni}^{2+}/\text{Ni}^{3+}$  and  $\text{Co}^{2+}/\text{Co}^{3+}$ .

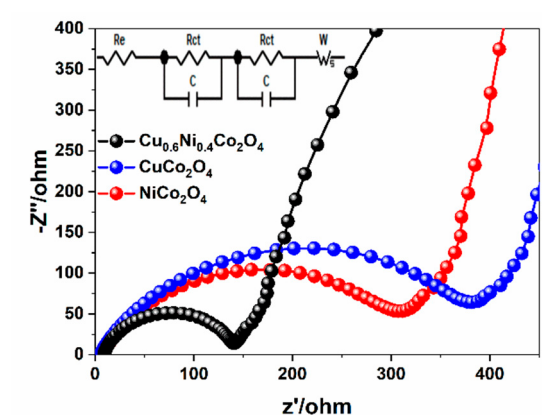


**Figure 8.** Nyquist plots for the three electrodes in the frequency range from 100 kHz to 0.01 Hz.

#### 4. Conclusions

In this work,  $\text{Cu}_{0.6}\text{Ni}_{0.4}\text{Co}_2\text{O}_4$  nanowires, with high electrochemical performance, have been synthesized by a simple and scalable hydrothermal approach. The material shows initial specific discharge and charge capacities of 1120 and 972  $\text{mAh g}^{-1}$  at current density of 50  $\text{mA g}^{-1}$ . After 50 cycles, its discharge capacity maintains 880  $\text{mAh g}^{-1}$ , and the coulombic efficiency is close to 100%. After a high current charge/discharge test, the reversible specific capacity can still be restored to 780  $\text{mAh g}^{-1}$  at 50  $\text{mA g}^{-1}$ , which is ca. 88% of the initial capacity. EIS and CV tests have proved that co-doping with appropriate amount of Cu and Ni could significantly enhance ion diffusion and electron conduction during charge-discharge process. We attribute the high performance to relatively low activation energy for electron transfer between  $\text{Cu}^{2+}$ ,  $\text{Ni}^{2+}/\text{Ni}^{3+}$  and  $\text{Co}^{2+}/\text{Co}^{3+}$ , the electronic conductivity and structure stability for  $\text{Cu}_{0.6}\text{Ni}_{0.4}\text{Co}_2\text{O}_4$  nanowires are improved greatly. Therefore, it is important to further research into other multi-component transition metal oxides as anode materials in lithium battery.

**Author Contributions:** Synthesis of the sample, writing—original draft preparation, J.L. (Junhao Li); investigation of the electrochemical performance, N.J.; characterization and analysis of the sample, J.L. (Jinyun Liao) and Y.F.; Supervision, funding acquisition and writing—review and editing, Q.L. and H.L. All authors have read and agreed to the published version of the manuscript.

**Funding:** This work was funded by the National Natural Science Foundation of China (Nos. 21606050, U1801257, 21975056), the Natural Science Foundation of Guangdong Province (No. 2018A030313859), Pearl River Science and Technology New Star Project (No. 201806010039), the Major Project of Fundamental and Application Research of the Department of Education of Guangdong Province (No. 2017KZDXM079), the Science and Technology Project of Huizhou City (No. 2017C0412028), the Natural Science Foundation of Huizhou University (No. 20180927172750326).

**Conflicts of Interest:** The authors declare no conflict of interest.

## References

1. Goodenough, J.B.; Park, K.S. The Li-ion rechargeable battery: A perspective. *J. Am. Chem. Soc.* **2013**, *135*, 1167–1176. [[CrossRef](#)]
2. Armand, M.; Tarascon, J.-M. Building better batteries. *Nature* **2008**, *451*, 652–657. [[CrossRef](#)]
3. Poizot, P.; Laruelle, S.; Gruegeon, S.; Dupont, L.; Tarascon, J.-M. Nano-sized transition-metal oxides as negative-electrode materials for lithium-ion batteries. *Nature* **2000**, *407*, 496–499. [[CrossRef](#)]
4. Reddy, M.V.; Subba, R.G.V.; Chowdari, B.V. Metal oxides and oxysalts as anode materials for Li ion batteries. *Chem. Rev.* **2013**, *113*, 5364–5457. [[CrossRef](#)]
5. Lou, X.W.; Deng, D.; Lee, J.Y.; Archer, L.A. Thermal formation of mesoporous single-crystal  $\text{Co}_3\text{O}_4$  nano-needles and their lithium storage properties. *J. Mater. Chem.* **2008**, *18*, 4397. [[CrossRef](#)]
6. Gu, D.; Li, W.; Wang, F.; Bongard, H.; Spliethoff, B.; Schmidt, W.; Weidenthaler, C.; Xia, Y.; Zhao, D.; Schüth, F. Controllable Synthesis of Mesoporous Peapod-like  $\text{Co}_3\text{O}_4$ @Carbon Nanotube Arrays for High-Performance Lithium-Ion Batteries. *Angew. Chem. Int. Ed.* **2015**, *54*, 7060–7064. [[CrossRef](#)] [[PubMed](#)]
7. Wu, Y.; Meng, J.; Li, Q.; Niu, C.; Wang, X.; Yang, W.; Li, W.; Mai, L. Interface-modulated fabrication of hierarchical yolk-shell  $\text{Co}_3\text{O}_4/\text{C}$  dodecahedrons as stable anodes for lithium and sodium storage. *Nano Res.* **2017**, *10*, 2364–2376. [[CrossRef](#)]
8. Yan, C.; Chen, G.; Zhou, X.; Sun, J.; Lv, C. Template-Based Engineering of Carbon-Doped  $\text{Co}_3\text{O}_4$  Hollow Nanofibers as Anode Materials for Lithium-Ion Batteries. *Adv. Funct. Mater.* **2016**, *26*, 1428–1436. [[CrossRef](#)]
9. Ma, Y.; He, J.; Kou, Z.; Elshahawy, A.M.; Hu, Y.; Guan, C.; Li, X.; Wang, J. MOF-Derived Vertically Aligned Mesoporous  $\text{Co}_3\text{O}_4$  Nanowires for Ultrahigh Capacity Lithium-Ion Batteries Anodes. *Adv. Mater. Interfaces* **2018**, *5*, 1800222. [[CrossRef](#)]
10. Wang, J.; Zhang, Q.; Li, X.; Xu, D.; Wang, Z.; Guo, H.; Zhang, K. Three-dimensional hierarchical  $\text{Co}_3\text{O}_4/\text{CuO}$  nanowire heterostructure arrays on nickel foam for high-performance lithium ion batteries. *Nano Energy* **2014**, *6*, 19–26. [[CrossRef](#)]
11. Guan, B.Y.; Yu, X.Y.; Wu, H.B.; Lou, X.W. Complex Nanostructures from Materials based on Metal-Organic Frameworks for Electrochemical Energy Storage and Conversion. *Adv. Mater.* **2017**, *29*. [[CrossRef](#)]
12. Dou, Y.; Xu, J.; Ruan, B.; Ruan, B.; Liu, Q.; Pan, Y.; Sun, Z.; Dou, S. Atomic Layer-by-Layer  $\text{Co}_3\text{O}_4$ /Graphene Composite for High Performance Lithium-Ion Batteries. *Adv. Energy Mater.* **2016**, *6*, 1501835. [[CrossRef](#)]
13. Huang, G.; Zhang, F.; Du, X.; Qin, Y.; Yin, D.; Wang, L. Metal Organic Frameworks Route to in Situ Insertion of Multiwalled Carbon Nanotubes in  $\text{Co}_3\text{O}_4$  Polyhedra as Anode Materials for Lithium-Ion Batteries. *ACS Nano* **2015**, *9*, 1592–1599. [[CrossRef](#)]
14. Hou, Y.; Li, J.; Wen, Z.; Cui, S.; Yuan, C.; Chen, J.  $\text{Co}_3\text{O}_4$  nanoparticles embedded in nitrogen-doped porous carbon dodecahedrons with enhanced electrochemical properties for lithium storage and water splitting. *Nano Energy* **2015**, *12*, 1–8. [[CrossRef](#)]
15. Li, Y.; Li, X.; Wang, Z.; Guo, H.; Li, T. Distinct impact of cobalt salt type on the morphology, microstructure, and electrochemical properties of  $\text{Co}_3\text{O}_4$  synthesized by ultrasonic spray pyrolysis. *J. Alloy. Compd.* **2017**, *696*, 836–843. [[CrossRef](#)]
16. Xu, G.L.; Li, J.-T.; Huang, L.; Lin, W.; Sun, S.G. Synthesis of  $\text{Co}_3\text{O}_4$  nano-octahedra enclosed by {111} facets and their excellent lithium storage properties as anode material of lithium ion batteries. *Nano Energy* **2013**, *2*, 394–402. [[CrossRef](#)]
17. Wang, D.; Yu, Y.; He, H.; Wang, J.; Zhou, W.; Abruna, H.D. Template-free synthesis of hollow-structured  $\text{Co}_3\text{O}_4$  nanoparticles as high-performance anodes for lithium-ion batteries. *ACS Nano* **2015**, *9*, 1775–1781. [[CrossRef](#)]
18. Wu, R.; Qian, X.; Rui, X.; Liu, H.; Yadian, B.; Zhou, K.; Weri, J.; Yan, Q.; Feng, X.Q.; Long, Y.; et al. Zeolitic imidazolate framework 67-derived high symmetric porous  $\text{Co}_3\text{O}_4$  hollow dodecahedra with highly enhanced lithium storage capability. *Small* **2014**, *10*, 1932–1938. [[CrossRef](#)]
19. Yu, K.; Pan, X.; Zhang, G.; Liao, X.; Zhou, X.; Yan, M.; Xu, L.; Mai, L. Nanowires in Energy Storage Devices: Structures, Synthesis, and Applications. *Adv. Energy Mater.* **2018**, *8*, 1802369. [[CrossRef](#)]
20. Xiong, S.; Chen, J.S.; Lou, X.W.; Zeng, H.C. Mesoporous  $\text{Co}_3\text{O}_4$  and  $\text{CoO}@C$  Topotactically Transformed from Chrysanthemum-like  $\text{Co}(\text{CO}_3)_{0.5}(\text{OH})_{0.11}\text{H}_2\text{O}$  and Their Lithium-Storage Properties. *Adv. Funct. Mater.* **2012**, *22*, 861–871. [[CrossRef](#)]

21. Yuan, C.; Wu, H.B.; Xie, Y.; Lou, X.W. Mixed transition-metal oxides: Design, synthesis, and energy-related applications. *Angew. Chem. Int. Ed.* **2014**, *53*, 1488–1504. [[CrossRef](#)]
22. Wei, T.Y.; Chen, C.H.; Chien, H.C.; Lu, S.Y.; Hu, C.C. A cost-effective supercapacitor material of ultrahigh specific capacitances: Spinel nickel cobaltite aerogels from an epoxide-driven sol-gel process. *Adv. Mater.* **2010**, *22*, 347–351. [[CrossRef](#)]
23. Hu, L.; Wu, L.; Liao, M.; Hu, X.; Fang, X. Electrical Transport Properties of Large, Individual NiCo<sub>2</sub>O<sub>4</sub> Nanoplates. *Adv. Funct. Mater.* **2012**, *22*, 998–1004. [[CrossRef](#)]
24. Alcntara, R.; Jaraba, M.; Lavela, P.; Tirado, J.L. NiCo<sub>2</sub>O<sub>4</sub> Spinel: First Report on a Transition Metal Oxide for the Negative Electrode of Sodium-Ion Batteries. *Chem. Mater.* **2002**, *14*, 2847–2848. [[CrossRef](#)]
25. Ma, F.-X.; Yu, L.; Xu, C.-Y.; Lou, X.W. Self-supported formation of hierarchical NiCo<sub>2</sub>O<sub>4</sub> tetragonal microtubes with enhanced electrochemical properties. *Energy Environ. Sci.* **2016**, *9*, 862–866. [[CrossRef](#)]
26. Shen, L.; Yu, L.; Yu, X.-Y.; Zhang, X.; Lou, X.W. Self-Templated Formation of Uniform NiCo<sub>2</sub>O<sub>4</sub> Hollow Spheres with Complex Interior Structures for Lithium-Ion Batteries and Supercapacitors. *Angew. Chem. Int. Ed.* **2015**, *127*, 1868–1872. [[CrossRef](#)]
27. Hu, H.; Guan, B.; Xia, B.; Lou, X.W. Designed Formation of Co<sub>3</sub>O<sub>4</sub>/NiCo<sub>2</sub>O<sub>4</sub> Double-Shelled Nanocages with Enhanced Pseudocapacitive and Electrocatalytic Properties. *J. Am. Chem. Soc.* **2015**, *137*, 5590–5595. [[CrossRef](#)]
28. Sharma, Y.; Sharma, N.; Rao, G.V.S.; Chowdari, B.V.R. Lithium recycling behaviour of nano-phase-CuCo<sub>2</sub>O<sub>4</sub> as anode for lithium-ion batteries. *J. Power Sources* **2007**, *173*, 495–501. [[CrossRef](#)]
29. Sharma, Y.; Sharma, N.; Subbarao, G.; Chowdari, B. Studies on spinel cobaltites, FeCo<sub>2</sub>O<sub>4</sub> and MgCo<sub>2</sub>O<sub>4</sub> as anodes for Li-ion batteries. *Solid State Ionics* **2008**, *179*, 587–597. [[CrossRef](#)]
30. Bai, J.; Li, X.; Liu, G.; Qian, Y.; Xiong, S. Unusual Formation of ZnCo<sub>2</sub>O<sub>4</sub> 3D Hierarchical Twin Microspheres as a High-Rate and Ultralong-Life Lithium-Ion Battery Anode Material. *Adv. Funct. Mater.* **2014**, *24*, 3012–3020. [[CrossRef](#)]
31. Lavela, P.; Tirado, J.L.; Vidal-Abarca, C. Sol-gel preparation of cobalt manganese mixed oxides for their use as electrode materials in lithium cells. *Electrochim. Acta* **2007**, *52*, 7986–7995. [[CrossRef](#)]
32. Jiang, F.; Su, Q.; Li, H.; Yao, L.; Deng, H.; Du, G. Growth of ultrafine CuCo<sub>2</sub>O<sub>4</sub> nanoparticle on graphene with enhanced lithium storage properties. *Chem. Eng. J.* **2017**, *314*, 301–310. [[CrossRef](#)]
33. Zhu, Y.; Cao, C.; Zhang, J.; Xu, X. Two-dimensional ultrathin ZnCo<sub>2</sub>O<sub>4</sub> nanosheets: General formation and lithium storage application. *J. Mater. Chem. A* **2015**, *3*, 9556–9564. [[CrossRef](#)]
34. Lu, D.; Liao, J.; Zhong, S.; Leng, Y.; Ji, S.; Wang, H.; Wang, R.; Li, H. Cu<sub>0.6</sub>Ni<sub>0.4</sub>Co<sub>2</sub>O<sub>4</sub> nanowires, a novel noble-metal-free catalyst with ultrahigh catalytic activity towards the hydrolysis of ammonia borane for hydrogen production. *Int. J. Hydrogen Energ.* **2018**, *43*, 5541–5550. [[CrossRef](#)]
35. Liu, L.; Wang, J.; Hou, Y.; Chen, J.; Liu, H.K.; Wang, J.; Wu, Y. Self-Assembled 3D Foam-Like NiCo<sub>2</sub>O<sub>4</sub> as Efficient Catalyst for Lithium Oxygen Batteries. *Small* **2016**, *12*, 602–611. [[CrossRef](#)] [[PubMed](#)]
36. Sun, S.; Wen, Z.; Jin, J.; Cui, Y.; Lu, Y. Synthesis of ordered mesoporous CuCo<sub>2</sub>O<sub>4</sub> with different textures as anode material for lithium ion battery. *Microporous Mesoporous Mater.* **2013**, *169*, 242–247. [[CrossRef](#)]
37. Chen, Y.; Zhu, J.; Qu, B.; Lu, B.; Xu, Z. Graphene improving lithium-ion battery performance by construction of NiCo<sub>2</sub>O<sub>4</sub>/graphene hybrid nanosheet arrays. *Nano Energy* **2014**, *3*, 88–94. [[CrossRef](#)]
38. Li, J.; Xiong, S.; Liu, Y.; Ju, Z.; Qian, Y. High Electrochemical Performance of Monodisperse NiCo<sub>2</sub>O<sub>4</sub> Mesoporous Microspheres as an Anode Material for Li-Ion Batteries. *ACS Appl. Mater. Int.* **2013**, *5*, 981–988. [[CrossRef](#)]
39. Xu, J.; He, L.; Xu, W.; Tang, H.; Liu, H.; Han, T.; Zhang, C.; Zhang, Y. Facile synthesis of porous NiCo<sub>2</sub>O<sub>4</sub> microflowers as high-performance anode materials for advanced lithium-ion batteries. *Electrochim. Acta* **2014**, *145*, 185–192. [[CrossRef](#)]
40. Wu, Z.; Pu, X.; Zhu, Y.; Jing, M.; Chen, Q.; Jia, X.; Ji, X. Uniform porous spinel NiCo<sub>2</sub>O<sub>4</sub> with enhanced electrochemical performances. *J. Alloy. Compd.* **2015**, *632*, 208–217. [[CrossRef](#)]
41. Lu, D.; Li, J.; Lin, C.; Liao, J.; Feng, Y.; Ding, Z.; Li, W.; Liu, Q.; Li, H. A Simple and Scalable Route to Synthesize Co<sub>x</sub>Cu<sub>1-x</sub>Co<sub>2</sub>O<sub>4</sub>@Co<sub>y</sub>Cu<sub>1-y</sub>Co<sub>2</sub>O<sub>4</sub> Yolk-Shell Microspheres, A High-Performance Catalyst to Hydrolyze Ammonia Borane for Hydrogen Production. *Small* **2019**, *15*, e1805460. [[CrossRef](#)] [[PubMed](#)]
42. Zhang, C.; Yu, J.-S. Morphology-Tuned Synthesis of NiCo<sub>2</sub>O<sub>4</sub>-Coated 3D Graphene Architectures Used as Binder-Free Electrodes for Lithium-Ion Batteries. *Chem. Eur. J.* **2016**, *22*, 4422–4430. [[CrossRef](#)] [[PubMed](#)]

43. Gao, G.; Wu, H.B.; Lou, X.W. Citrate-Assisted Growth of NiCo<sub>2</sub>O<sub>4</sub> Nanosheets on Reduced Graphene Oxide for Highly Reversible Lithium Storage. *Adv. Energy Mater.* **2014**, *4*, 1400422. [[CrossRef](#)]
44. Zhu, J.; Xu, Z.; Lu, B. Ultrafine Au nanoparticles decorated NiCo<sub>2</sub>O<sub>4</sub> nanotubes as anode material for high-performance supercapacitor and lithium-ion battery applications. *Nano Energy* **2014**, *7*, 114–123. [[CrossRef](#)]
45. Guo, W.; Sun, W.; Wang, Y. Multi-Layer CuO@NiO Hollow Spheres: Microwave-Assisted Metal-Organic-Framework Derivation and Highly Reversible Structure-Matched Stepwise Lithium Storage. *ACS Nano* **2015**, *9*, 11462–11471. [[CrossRef](#)] [[PubMed](#)]
46. Sun, S.; Zhao, X.; Yang, M.; Wu, L.; Wen, Z.; Shen, X. Hierarchically ordered mesoporous Co<sub>3</sub>O<sub>4</sub> materials for high performance Li-ion batteries. *Sci. Rep.* **2016**, *6*, 19564. [[CrossRef](#)]



© 2020 by the authors. Licensee MDPI, Basel, Switzerland. This article is an open access article distributed under the terms and conditions of the Creative Commons Attribution (CC BY) license (<http://creativecommons.org/licenses/by/4.0/>).